

# Stokes imaging spectropolarimeter based on channeled polarimetry with full-resolution spectra and aliasing reduction

CHUNMIN ZHANG,<sup>1</sup> NAICHENG QUAN,<sup>2,\*</sup> AND TINGKUI MU<sup>1</sup>

<sup>1</sup>Institute of Space Optics, Xi'an Jiaotong University, Xi'an 710049, China

<sup>2</sup>School of Materials Science and Engineering, Xi'an University of Technology, Xi'an 710048, China

\*Corresponding author: quanncx@hotmail.com

Received 3 April 2018; revised 12 June 2018; accepted 14 June 2018; posted 15 June 2018 (Doc. ID 327503); published 18 July 2018

A Stokes channeled interference imaging spectropolarimeter with full-resolution spectra and aliasing reduction is presented. The sensor uses a Wollaston prism, a Savart polariscope, and a linear analyzer as a birefringent interferometer, along with two high-order retarders to incorporate channeled polarimetry employing a tempo-spatially mixed modulated mode with no internal moving parts and offering a robust system. The performance of the system is verified through laboratory tests. Compared with the previous sensors, the most significant advantage of the described instrument is that the reconstructed spectra retain the resolution of the interferometer, and the errors in the reconstructed spectral resolved polarization state caused by aliasing between the interference channels are suppressed effectively. Additionally, the advantages of the interferometer are maintained, such as compact structure and high optical throughput. © 2018 Optical Society of America

**OCIS codes:** (110.4234) Multispectral and hyperspectral imaging; (120.6200) Spectrometers and spectroscopic instrumentation; (260.5430) Polarization; (300.6300) Spectroscopy, Fourier transforms.

<https://doi.org/10.1364/AO.57.006128>

## 1. INTRODUCTION

An imaging spectropolarimeter (ISP) can acquire the spatial, spectral, and polarization information of targets simultaneously and improve the ability to effectively recognize the target with preferable accuracy [1–4]. The data sets obtained by ISP are 3D spatial and spectral data cubes of the Stokes parameters,  $S_0(\sigma)$ ,  $S_1(\sigma)$ ,  $S_2(\sigma)$ , and  $S_3(\sigma)$  [ $S_0(\sigma)$  is the total intensity of the light, while  $S_1(\sigma)$  denotes the part of 0° linear polarized light over 90°,  $S_2(\sigma)$  for +45° over −45°, and  $S_3(\sigma)$  for right circular over left circular,  $\sigma$  is spectral variable]. These four parameters can describe the complete polarization state of light at a given spectral band [4].

The ISP device has been rapidly developed within the past 10 years and is widely used in many fields, including biomedical optics, astronomy, remote sensing, and other scientific areas [5]. ISPs using rotating polarization elements, electrically controllable components, and microretarder or micropolarizer arrays generally suffer from vibration, electrical noise, heat generation, and alignment difficulty [6]. Another attractive method is the channeled polarimetric technique by which all the spectrally resolved Stokes parameters can be acquired at once without movable polarization components or microcomponents [7]. Based on this concept, the channeled polarimetric

technique is incorporated into a different interference imaging spectrometer (CIISP), which has unique benefits due to the throughput (Jacquinot) and multiplex (Fellgett) advantages [8–15]. Because the recorded interferogram usually contains more than three interference channels, the spectral resolution of each reconstructed Stokes parameters is lower than that of the interferometer. Besides, there is obvious aliasing among the fringe patterns of different Stokes parameters, when some narrowband spectra are measured by such sensor. By using the aperture division polarimeter based on Wollaston prisms, we can feed the four polarization spectra into the interference imaging spectrometer simultaneously [16]. However, the system can be only used for detecting the linear Stokes parameters.

In this paper, we propose a Stokes imaging spectropolarimeter based on channeled polarimetry with full-resolution spectra and aliasing reduction (FSRCIISP), employing a tempo-spatially mixed modulated mode without internal moving parts, electrically controllable or microcomponents, the full spectrally resolved Stokes parameters, spectral, and spatial information of a scene can be acquired simultaneously. Furthermore, the reconstructed spectra  $S_0(\sigma)$  retain the spectral resolution of the interferometer and the reconstructed errors in the spectra  $S_1(\sigma) \sim S_3(\sigma)$  caused by aliasing are

suppressed effectively. We describe the configuration and theoretical model of the FSRCIISP in Section 2. Section 3 presents the laboratory data from the FSRCIISP and discusses the results, while our conclusion is contained in Section 4.

## 2. SENSOR CONFIGURATION AND THEORETICAL MODEL

### A. Sensor Configuration

The layout of the proposed FSRCIISP is depicted in Fig. 1. The high-order retarders  $R_1$  and  $R_2$  with fast axes oriented at  $0^\circ$  and  $45^\circ$  relative to the  $x$  axis are installed behind the fore optics. These are followed by a Wollaston prism (WP), a Savart polariscope (SP), a linear analyzer (LA), a reimaging lens  $L_2$ , and a charge-coupled device (CCD). The principal sections of the two prisms in WP are parallel to the  $x$  and  $y$  axes, respectively. The principal sections of the two plates in SP are at  $45^\circ$  and  $-45^\circ$  with the  $x$  axis, respectively. The polarization direction of the LA is parallel to the  $x$  axis. The CCD is placed on the back focal plane of  $L_2$ . The field stop  $M$  is placed on the intermediate image plane of  $L_0$  to prevent the pair of interferograms from overlapping on the single CCD camera.

Light from a scene is collected and imaged on the field stop  $M$  by lens  $L_0$  and then collimated by lens  $L_1$ . The parallel light passes through the pair of birefringent retarders,  $R_1$  and  $R_2$ . The output beam from  $R_2$  is angularly split into two orthogonally polarized beams by WP in the plane perpendicular to the  $x-z$  plane. Each of beams is parallel laterally sheared by the SP. The LA extracts the linearly polarized component that is parallel to the  $x$  axis with equal amplitude. When each pair of the sheared beams is reunited on the back focal plane of the  $L_2$ , a pair of interference images in the spatial domain is recorded by the CCD camera. The optical path difference (OPD) is supplied by the shear of SP. The complete interferogram for the same object pixel is collected by employing the tempo-spatially mixed modulation model (windowing mode) [15,17,18]. The system acquires a full 2D image per frame, with successive frames associated with different OPD by scanning across a scene. The selected magnitude, range, and spacing of the OPD determine the spectral range and resolution.

A photograph of the core optics in FSRCIISP is shown in Fig. 2. The FSRCIISP system is relatively compact ( $\sim 100$  mm long, not including the imaging optics). The birefringent elements used in FSRCIISP are made of two kinds of materials. The calcite prism works as a Glan–Taylor analyzer (extinction ratio  $\geq 10^5$ ) LA, the beam splitter WP and SP. The quartz prisms are used for the two high-order retarders. The apex angle of wedge in LA is nominally  $39.7^\circ$ . The dimensions of WP are  $20 \text{ mm} \times 20 \text{ mm} \times 5 \text{ mm}$  with an apex angle of  $7.8^\circ$ . The dimensions of SP are  $20 \text{ mm} \times 20 \text{ mm} \times 13 \text{ mm}$ . According to the Nyquist sampling theorem, the sampling interval of the

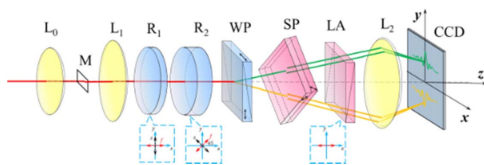


Fig. 1. Optical layout of FSRCIISP.

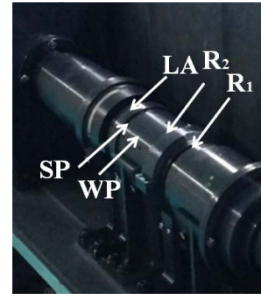


Fig. 2. Photograph of the core optics in FSRCIISP.

interferogram is no more than  $\delta\Delta = \lambda_{\min}/2 = 0.2 \text{ } \mu\text{m}$ . The maximum OPD  $\Delta_{\max}$  is effectively limited by the Nyquist criterion that requires at least two data points per fringe period. The interferogram is symmetrically recorded about the zero OPD; the maximum OPD  $\Delta_{\max}$  supplied by SP is  $51.2 \text{ } \mu\text{m}$ . The highest spectral resolution is  $\delta\lambda = \lambda^2/2\Delta_{\max}$ , which is about  $1.6 \text{ nm}$  at the wavelength of  $400 \text{ nm}$ .  $R_1$  and  $R_2$  are cylindrical  $35 \text{ mm}$  diameter elements, with thicknesses of  $1.6$  and  $3.2 \text{ mm}$ , respectively. Fabrication tolerance of the apex angles of wedges and dimensions of the elements are  $\pm 0.1^\circ$  and  $0.1 \text{ mm}$ , respectively. A  $12.3 \text{ mm} \times 6.1 \text{ mm}$  field stop is located at the fore focal plane of  $L_1$  to prevent the two interferograms from overlapping on the CCD camera. Note that all birefringent elements are antireflection (AR) coated for wavenumber  $\sigma = 12500\text{--}25000 \text{ cm}^{-1}$  (wavelength  $\lambda = 400\text{--}800 \text{ nm}$ ), providing  $>93\%$  transmission through the birefringent interferometer. A commercial monochromatic Sarnoff CAM512 CCD camera is used to take the interferograms and images of the targets. The camera uses a  $512 \times 512$  element FPA with a pixel size of  $18 \text{ } \mu\text{m}$ , and the maximum frame rate can reach  $250 \text{ Hz}$  to ensure speed of data collection.

### B. Theoretical Model

A Savart polariscope, which plays the role of a lateral shearing beam splitter, is the key element of the spectrometer. It is used to separate the input beam into two coherent interfering beams and produce phase-delay between them. The principal section of left plate of SP in the system is oriented at  $45^\circ$  relative to the  $y-z$  plane, the fringe pattern is similar to that in the Young's double slit setup under paraxial condition and is a straight line parallel to the  $x$  axis [15,16]. The OPD produced by the SP is given by

$$\Delta(\sigma, x) = d(\sigma)x/f, \quad (1)$$

where  $d(\sigma) = \sqrt{2t[n_o^2(\sigma) - n_e^2(\sigma)]/[n_o^2(\sigma) + n_e^2(\sigma)]}$  is the lateral displacement,  $t$  is the thickness of a single plate in SP,  $n_o$  and  $n_e$  are ordinary and extraordinary refractive indices of the uniaxial crystal, and  $f$  is the focal length of the lens  $L_2$ . As described above, the WP acts as orthogonal polarizers, and the corresponding polarization directions are parallel and perpendicular to  $x$  axis, respectively. Assuming that light from the scene has a broadband spectrum with wavenumber  $\sigma$  from  $\sigma_s$  to  $\sigma_e$ , by using the Mueller calculus, the pair of fringe patterns  $I_1(\Delta)$  and  $I_2(\Delta)$  can be described as

$$I_1(\Delta) = K_1 \int_{\sigma_i}^{\sigma_e} \cos \varphi_{SP} \times \left[ \begin{aligned} &\frac{S_0}{2} + \frac{1}{4} S_1 e^{i\varphi_2} + \frac{1}{4} S_1 e^{-i\varphi_2} + \frac{S_2 - iS_3}{8} e^{i(\varphi_1 - \varphi_2)} \\ &+ \frac{S_2 + iS_3}{8} e^{-i(\varphi_1 - \varphi_2)} + \frac{-S_2 + iS_3}{8} e^{i(\varphi_1 + \varphi_2)} \\ &+ \frac{-S_2 - iS_3}{8} e^{-i(\varphi_1 + \varphi_2)} \end{aligned} \right] d\sigma, \quad (2)$$

$$I_2(\Delta) = K_2 \int_{\sigma_i}^{\sigma_e} \cos \varphi_{SP} \times \left[ \begin{aligned} &-\frac{S_0}{2} + \frac{1}{4} S_1 e^{i\varphi_2} + \frac{1}{4} S_1 e^{-i\varphi_2} + \frac{S_2 - iS_3}{8} e^{i(\varphi_1 - \varphi_2)} \\ &+ \frac{S_2 + iS_3}{8} e^{-i(\varphi_1 - \varphi_2)} + \frac{-S_2 + iS_3}{8} e^{i(\varphi_1 + \varphi_2)} \\ &+ \frac{-S_2 - iS_3}{8} e^{-i(\varphi_1 + \varphi_2)} \end{aligned} \right] d\sigma. \quad (3)$$

In Eqs. (2) and (3), the background intensity and constant offset have been neglected because they do not provide any useable spectral information in the Fourier transform.  $K_1$  and  $K_2$  are amplitude coefficients introduced by the system. The phase terms are presented as  $\varphi = 2\pi\Delta\sigma$ ,  $\varphi_1 = 2\pi B(\sigma)d_1\sigma$ , and  $\varphi_2 = 2\pi B(\sigma)d_2\sigma$ , where  $B(\sigma)$  is the birefringence of the birefringent crystal, and  $d_1$  and  $d_2$  are thicknesses of the retarders  $R_1$  and  $R_2$ , respectively. Performing the integration over  $\sigma$ , Eq. (2) and Eq. (3) can be rewritten as

$$I_1(\Delta) = K_1 \times \left[ \begin{aligned} &C_0(\Delta) + C_2(\Delta - L_2) + C_2^*(\Delta + L_2) + C_1(\Delta + L_1 - L_2) \\ &+ C_1^*(\Delta - L_1 + L_2) + C_3(\Delta - L_1 - L_2) + C_3^*(\Delta + L_1 + L_2) \end{aligned} \right], \quad (4)$$

$$I_2(\Delta) = K_2 \times \left[ \begin{aligned} &-C_0(\Delta) + C_2(\Delta - L_2) + C_2^*(\Delta + L_2) + C_1(\Delta + L_1 - L_2) \\ &+ C_1^*(\Delta - L_1 + L_2) + C_3(\Delta - L_1 - L_2) + C_3^*(\Delta + L_1 + L_2) \end{aligned} \right]. \quad (5)$$

Here,  $L_1$  and  $L_2$  denote the OPD introduced by  $R_1$  and  $R_2$  in the central wavenumber, respectively. It can be seen that the fringe patterns  $I_1(\Delta)$  and  $I_2(\Delta)$  are separated into seven channels, centered at  $\Delta = 0, \pm(L_1 - L_2), \pm L_2, \pm(L_1 + L_2)$ . These channels can be seen from two real interference fringes collected with the FSRCIISP shown in Fig. 3, where a 60° linear incident polarization state and a broadband source were used to produce the interferogram. Each channel contained in  $I_1(\Delta)$  and  $I_2(\Delta)$  occupied the total OPD that makes an inevitable aliasing between the channels exist. For the conventional channelled

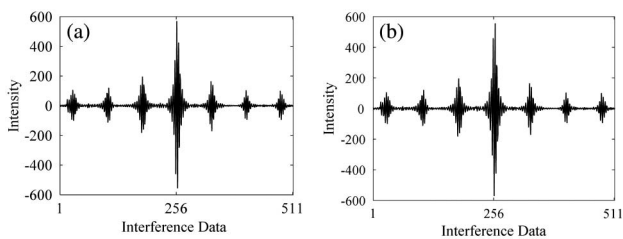


**Fig. 3.** Interferogram selected by FSRCIISP for a 60° linear incident polarization state. The seven channels in the interferogram are separated in OPD space by the retardations  $\varphi_1$  and  $\varphi_2$ . (a)  $I_1(\Delta)$ . (b)  $I_2(\Delta)$ .

interference imaging spectropolarimeter (CIISP), the reconstruction is performed by filtering the desired interference fringes around the center burst of each channel and is followed by Fourier transformation [15]. The spectral resolution of the spectra  $S_0(\sigma)$  reconstructed by CIISP is 1/7 of the interference imaging spectropolarimeter, and the reconstructed  $S_1(\sigma)$ ,  $S_2(\sigma)$ , and  $S_3(\sigma)$  spectra contain unavoidable errors caused by aliasing between the channels.

Note that  $C_0(\Delta)$  contained in  $I_1(\Delta)$  and  $I_2(\Delta)$  recorded by FSRCIISP displays a 180° carrier frequency phase shift relative to each other. This enables removal of the channels that contain  $S_1(\sigma)$ ,  $S_2(\sigma)$ , and  $S_3(\sigma)$  when the two fringe patterns are weighted and subtracted:

$$I_1(\Delta) - \frac{K_1}{K_2} I_2(\Delta) \propto \int_{\sigma_i}^{\sigma_e} \cos \varphi_{SP} S_0 d\sigma. \quad (6)$$

Equation (6) is a full-resolution fringe pattern, as would be collected by the spectrometer that removed the retarders. The aliasing in other channels caused by  $S_0(\sigma)$  can be removed by

$$I_1(\Delta) - \frac{K_1}{K_2} I_2(\Delta) \propto \left[ \begin{aligned} &C_2(z - L_2) + C_2^*(z + L_2) + C_1(z + L_1 - L_2) \\ &+ C_1^*(z - L_1 + L_2) + C_3(z - L_1 - L_2) \\ &+ C_3^*(z + L_1 + L_2) \end{aligned} \right]. \quad (7)$$

Taking Fourier transformation to Eq. (6), filtering the desired channels  $C_1^*$  and  $C_2^*$  in Eq. (7) and followed by Fourier transform, the spectrally resolved Stokes parameters of the target can be demodulated as follows:

$$\mathfrak{F}\left\{I_1(\Delta) - \frac{K_1}{K_2} I_2(\Delta)\right\} = S_0(\sigma), \quad (8)$$

$$\mathfrak{F}\{C_1^*\} = \frac{1}{2} |S_1(\sigma)| \exp\{i[\varphi_2(\sigma) + \arg\{S_1(\sigma)\}]\}, \quad (9)$$

$$\mathfrak{F}\{C_2^*\} = \frac{1}{4} |S_{23}(\sigma)| \exp\{i[\varphi_2(\sigma) - \varphi_1(\sigma) + \arg\{S_{23}(\sigma)\}]\}, \quad (10)$$

where  $S_{23}(\sigma) = S_2(\sigma) + iS_3(\sigma)$  and  $\arg$  stands for the operator to take the argument. In Eqs. (8) and (9), only  $S_0(\sigma)$  can be demodulated directly, while  $S_1(\sigma)$ ,  $S_2(\sigma)$ , and  $S_3(\sigma)$  are still modulated by  $\varphi_1$  and  $\varphi_2$ . The phase factors in  $C_1^*$  and  $C_2^*$  can be calibrated out to reconstruct the full Stokes parameters described in Section 3.

The interference fringe  $I_2(\Delta)$  is weighted by the ratio of amplitude coefficient (RAC)  $K_1/K_2$  before being added and subtracted to  $I_1(\Delta)$  to generate a full spectral resolution interference fringe and the interference fringe without the dominated aliasing, respectively. RAC can be measured by collected two interference fringes  $I_1^u(\Delta)$  and  $I_2^u(\Delta)$  corresponding to unpolarized incident light as follows:

$$I_1^u(\Delta) = K_1 \int_{\sigma_i}^{\sigma_e} \cos \varphi_{SP} \frac{S_0}{2} d\sigma, \quad (11)$$

$$I_2^u(\Delta) = -K_2 \int_{\sigma_i}^{\sigma_e} \cos \varphi_{SP} \frac{S_0}{2} d\sigma, \quad (12)$$

$$\frac{K_1}{K_2} = \frac{I_1^u(\Delta)}{I_2^u(\Delta)}. \quad (13)$$

### 3. EXPERIMENT AND RESULTS

#### A. Experiment Setup and Calibration

##### 1. Calibration of Ratio of Amplitude Coefficient

We carried out a demonstration experiment to prove the feasibility of the proposed FSRCIISP; the setup is illustrated in Fig. 4. The polychromatic light is conducted to an integrating sphere to generate uniform and unpolarized light. A polarization state generator (PSG) consisting of different polarization elements is used to generate controllable polarization states.

In order to determine accurate RAC and reconstruct the complete Stokes parameters from the scene without including background effects, detector offsets must be accounted for via a relative radiometric calibration of the sensor. Because the fringe pattern is a straight line, which is parallel to the column pixels, the relative radiometric calibration was done by pixels in each column, which ideally have the same brightness without the pixels corresponding to the image of the field stop [16]. To generate unpolarized radiation, the PSG was removed from the setup. The dual interferograms  $I_1^u(\Delta)$  and  $I_2^u(\Delta)$  corresponding to Eq. (11) and Eq. (12) were recorded by FSRCIISP. Figures 5(a) and 5(b) show the simultaneously captured dual interferograms of the unpolarized radiation from an integrating sphere before and after relative radiometric calibration, respectively. The channeled interferograms with a  $180^\circ$  carrier frequency phase shift of  $C_0$  relative to each other separated by the field stop were distributed symmetrically on a single CCD. The two interferograms occupy  $253 \times 512$  pixels, and the other pixels are occupied by the image of the field stop.

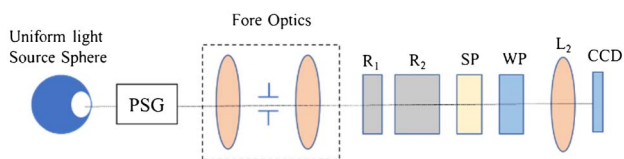


**Fig. 4.** Experiment setup for laboratory testing of the FSRCIISP.

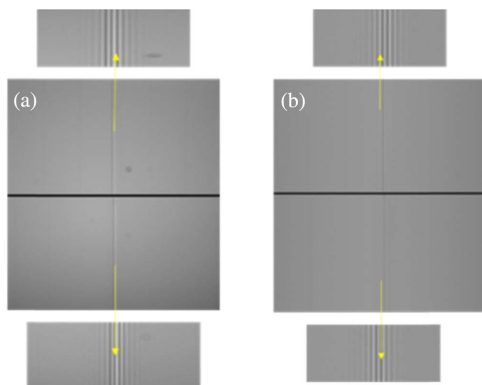


**Fig. 5.** Dual interferograms of the unpolarized radiation from integrating sphere (a) before relative radiometric calibration and (b) after relative radiometric calibration.

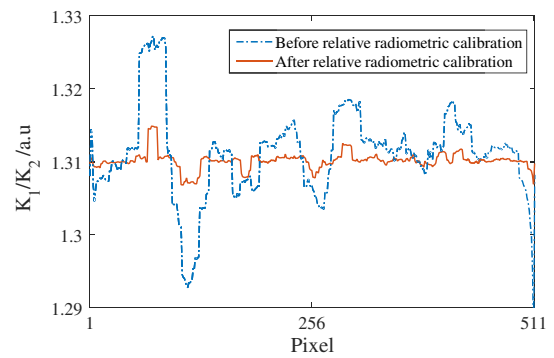


**Fig. 6.** Calibrated ratio of amplitude coefficient.

The nonuniformity of the CCD image caused by manufacturing defects and vignetting artifacts of the complete instrument has been improved, as shown in Fig. 5(b). According to Eqs. (11)–(13), the acquired RAC of two arbitrarily selected rows from the dual interferograms are shown in Fig. 6. As can be seen, the deviations in RAC have an average reduction of 42.8% after relative radiometric calibration of the sensor.

To verify the effectiveness of the calibrated RAC on the acquisition of the full-resolution fringe pattern and the fringe pattern without dominant aliasing, radiation with  $0^\circ$  linear polarization state was recorded by the sensor. Figures 7(a) and 7(b) show the fringe pattern corresponding to Eq. (6) and Eq. (7), respectively. Compared with the fringe pattern acquired by CIISP, which is described by Eq. (4) and shown in Fig. 7(c), the strength of the fringe patterns includes effective spectral data in both Figs. 7(a) and 7(b) increased nearly twice and the average aliasing between the channels in Fig. 7(b) decreased by almost 52.3%.

##### 2. Spectral Calibration

The spectral calibration was performed using a monochromatic light as the calibration source with a known wavenumber.

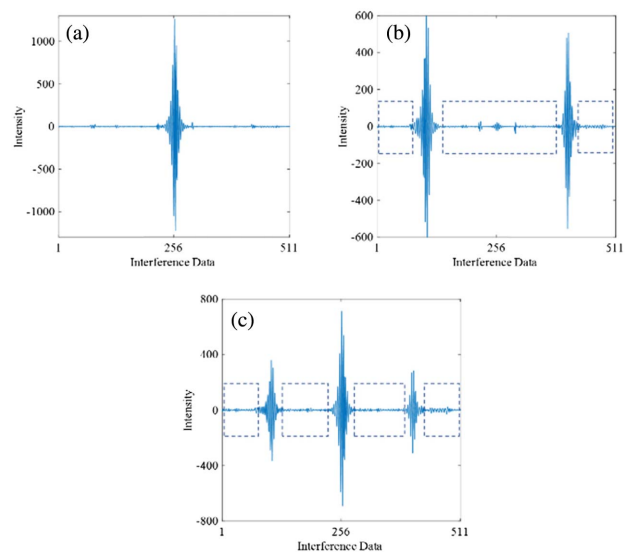


**Fig. 7.** Fringe pattern corresponding to  $0^\circ$  linear polarization state (a) full-resolution fringe pattern, (b) fringe pattern without dominant aliasing, and (c) original channeled fringe pattern.



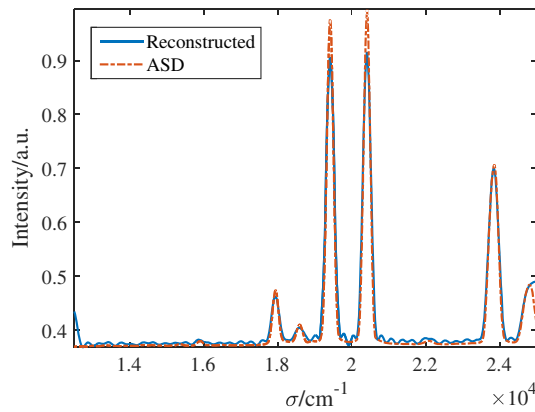


Fig. 8. Spectral calibration results.

The spectral axis of the reconstructed spectra is scaled with much monochromatic light produced from an argon ion tunable laser, and the reconstructed polychromatic light is calibrated with that recorded by an Analytical Spectral Devices, Inc. (ASD) spectroradiometer. Because the lateral shear  $d$  is the function of the extraordinary and ordinary indices, the OPD varies as a function of wavelength. Therefore, the dispersion of the birefringent crystal is compensated using the Sellmeier equation of calcite and a reference wavelength [15]. Figure 8 shows the reconstructed spectra of a Mercury lamp by FSRCIISP after spectral calibration. As can be seen, the reconstructed wavelengths of spectral characteristic peaks of a Mercury lamp coincide with the values measured by the commercial ASD.

### 3. Polarimetric Calibration

To determine the carrier frequencies' phase factors,  $\varphi_1$  and  $\varphi_2$ , and demodulate the unknown Stokes parameters, a calibration routine must be implemented. Two effective techniques can perform this kind of polarimetric calibration [7,19]. One is a reference beam calibration technique that involves measuring a known reference polarization state to correct for the modulating phase factors. The other is a self-calibration technique that appropriates for retarders in the presence of thermal fluctuations, and no reference beam is needed. Because self-calibration has an underlying assumption that both retarders are in thermal equilibrium that leads to uncertainty in the calibration, the reference beam calibration technique was implemented for FSRCIISP. The reference beam calibration technique was performed with a broadband (12500–25000  $\text{cm}^{-1}$ ) source uniformly linearly polarized at  $22.5^\circ$  relative to the horizontal ( $y$  axis) that provides large amplitude modulations in both the  $C_1^*$  and  $C_2^*$  channels. To provide the uniform reference polarization across the FOV, a Glan–Taylor prism polarizer was placed directly in front of  $R_1$  with its transmission-axis oriented at  $22.5^\circ$ . To verify the results of polarimetric calibration, the polarization states generated at various rotation angles of the polarizer from  $0^\circ$  to  $180^\circ$  are tested. There constructed results of the normalized Stokes parameters obtained as a function of polarizer rotation angle and wavenumber, portrayed in contour plots, can be seen in Fig. 9. Note that the contours of the data in Figs. 9(a) and 9(b) should ideally consist of straight lines for

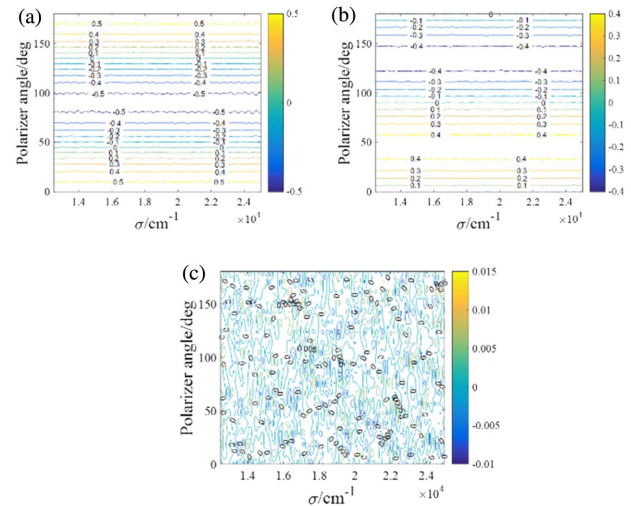


Fig. 9. Contour plots of the reconstructed results for the normalized Stokes parameters (a)  $S_1(\sigma)$ , (b)  $S_2(\sigma)$ , and (c)  $S_3(\sigma)$ .

$S_1(\sigma)$  and  $S_2(\sigma)$ ; the error is increased at the edges of the band due to the low intensity of the input radiation in the short wavelength band. Figure 9(c) shows the error distribution in the reconstruction of  $S_3(\sigma)$ . The RMS error calculations are performed over the 12500–25000  $\text{cm}^{-1}$  ( $\lambda = 400 \sim 800$  nm) spectral band relative to the known input states; the results show that the average RMS error in each normalized Stokes parameter is given by  $\epsilon_{S_1}^{\text{rms}} = 2.76\%$ ,  $\epsilon_{S_2}^{\text{rms}} = 3.43\%$ , and  $\epsilon_{S_3}^{\text{rms}} = 1.39\%$ .

### B. Experiment Results

Now, the measurement of any spectrally resolved Stokes parameters is ready. By replacing the rotatable polarizer with a PSG consists of a fixed horizontal polarizer and an achromatic quarter-wave plate with fast axes orientations  $\beta$  at  $30^\circ$  and  $60^\circ$  relative to the horizontal, we measure the dual interferograms simultaneously. The interferograms after background elimination are illustrated in Figs. 10 and 11. As can be seen, the seven channels are separated completely with equal intervals of  $12.8 \mu\text{m}$  in the OPD domain. According to Eq. (6), the full-resolution fringe pattern of spectra  $S_0(\sigma)$  can be acquired by the two fringe patterns weighted and subtracted.

The spectra  $S_0(\sigma)$  reconstructed by filtering the  $C_0$  channel corresponding to CIISP reconstruction is shown in Fig. 12, while Fig. 13 shows the reconstructed spectra through a

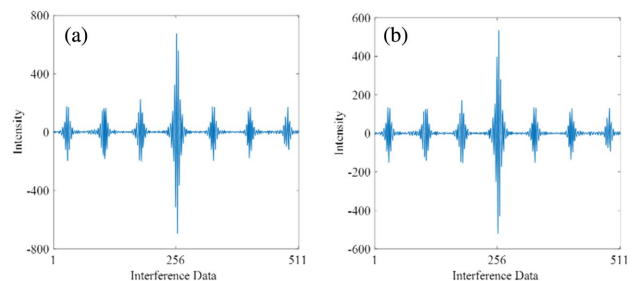
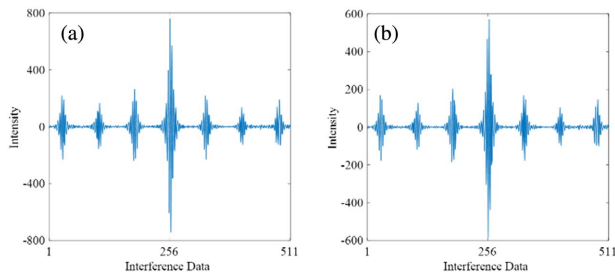
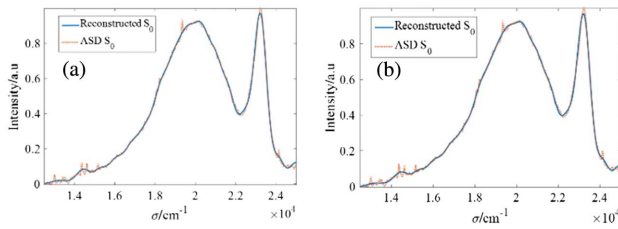


Fig. 10. Fringe patterns with  $180^\circ$  carrier frequency phase shift of  $C_0$  relative to each other after background elimination when  $\beta = 30^\circ$  (a)  $I_1(\Delta)$  and (b)  $I_2(\Delta)$ .



**Fig. 11.** Fringe patterns with  $180^\circ$  carrier frequency phase shift of  $C_0$  relative to each other after background elimination when  $\beta = 60^\circ$  (a)  $I_1(\Delta)$  and (b)  $I_2(\Delta)$ .



**Fig. 12.**  $S_0(\sigma)$  reconstructed by CIISP (a)  $\beta = 30^\circ$  and (b)  $\beta = 60^\circ$ . Solid and dashed curves show the experimental and theoretical values, respectively.

full-resolution fringe pattern. Because the dispersion of the birefringent crystal for fabricating the SP is compensated using the Sellmeier equation, the two reconstructed  $S_0(\sigma)$  are consistent with the incident spectra measured by ASD. Noting that the *OPD* of the filtered  $C_0$  channel is restricted to the area close to the center burst, the spectral resolution of  $S_0(\sigma)$  is limited, which makes the characteristic spectral lines in  $14360 \text{ cm}^{-1}$  and  $19340 \text{ cm}^{-1}$  of the mercury lamp unresolvable. The normalized spectral resolved Stokes parameters reconstructed by CIISP and FSRCIISP are shown in Fig. 14 and Fig. 15, respectively. An obvious reduction of the vibrations throughout the wavenumber range of the FSRCIISP reconstruction occurs due to removing the full resolution  $S_0(\sigma)$  interferogram from the channels.

Performing an RMS error calculation on the FSRCIISP reconstructed data spanning the  $12500\text{--}25000 \text{ cm}^{-1}$  waveband, we find  $\epsilon_{S1}^{\text{rms}} = 1.93\%$ ,  $\epsilon_{S2}^{\text{rms}} = 2.48\%$ , and  $\epsilon_{S3}^{\text{rms}} = 2.36\%$  for  $\beta$  equals  $30^\circ$  and  $\epsilon_{S1}^{\text{rms}} = 2.08\%$ ,  $\epsilon_{S2}^{\text{rms}} = 2.67\%$ , and  $\epsilon_{S3}^{\text{rms}} = 2.49\%$  for  $\beta$  equals  $60^\circ$ , respectively. Conversely, the CIISP

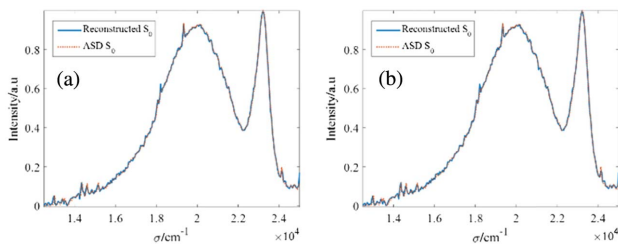


**Fig. 13.**  $S_0(\sigma)$  reconstructed by FSRCIISP (a)  $\beta = 30^\circ$  and (b)  $\beta = 60^\circ$ . Solid and dashed curves show the experimental and theoretical values, respectively.

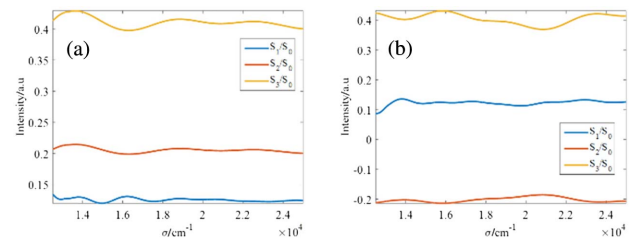


**Fig. 14.** Normalized Stokes parameters reconstructed by CIISP (a)  $\beta = 30^\circ$  and (b)  $\beta = 60^\circ$ .

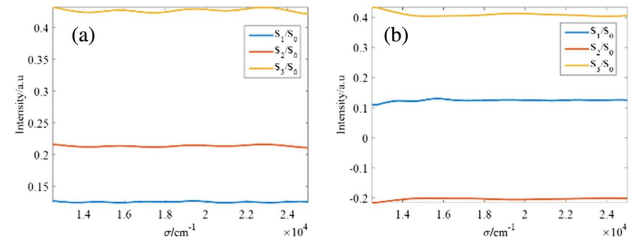


**Fig. 15.** Normalized Stokes parameters reconstructed by FSRCIISP (a)  $\beta = 30^\circ$  and (b)  $\beta = 60^\circ$ .

reconstructions demonstrate little similarity to the input polarization state and are subject to significant error across the same band with  $\epsilon_{S1}^{\text{rms}} = 6.75\%$ ,  $\epsilon_{S2}^{\text{rms}} = 8.63\%$ , and  $\epsilon_{S3}^{\text{rms}} = 9.04\%$  for  $\beta$  equals  $30^\circ$ , and  $\epsilon_{S1}^{\text{rms}} = 7.12\%$ ,  $\epsilon_{S2}^{\text{rms}} = 8.24\%$ , and  $\epsilon_{S3}^{\text{rms}} = 10.52\%$  for  $\beta$  equals  $60^\circ$ , respectively. These results further demonstrate the validity of FSRCIISP, with errors reduced by factors of 3 to 4 for the individual Stokes parameters.

## 4. CONCLUSION

In this paper, we presented a Stokes channeled interference imaging spectropolarimeter with full-resolution spectra and aliasing reduction. The sensor uses a Wollaston prism, a Savart polariscope, and a linear analyzer as a birefringent interferometer, along with two high-order retarders to incorporate channeled polarimetry employing a tempo-spatially mixed modulated mode with no internal moving parts and offers a robust system. Compared with the conventional channeled imaging interference spectropolarimeter, the major advantage of FSRCIISP is that it can acquire two sets of channeled fringe patterns of the same target simultaneously with a  $180^\circ$  carrier frequency phase shift of the  $S_0(\sigma)$  channel relative to each other, the reconstructed  $S_0(\sigma)$  spectra retain the resolution of the spectrometer, and the errors in the reconstructed polarimetric spectrum  $S_1(\sigma)$ ,  $S_2(\sigma)$ , and  $S_3(\sigma)$  caused by  $S_0(\sigma)$  are suppressed effectively. Furthermore, all of the incident light can pass through the WP due to its capability of converting orthogonally polarized light completely, and the optical efficiency of the system will be two times that of the birefringent interferometer using the general polarizer with the capability of blocking the cross-polarized component. The Savart-type interferometer used in the system also brings the FSRCIISP advantages of high optical throughput and broad wavelength range.

**Funding.** Scientific Research Support Program for New Teachers of Xi'an University of Technology (101-256081706); National Natural Science Foundation of China (NSFC) (61775176, 61405153).

**Acknowledgment.** We thank the anonymous reviewers for their helpful comments and constructive suggestions.

## REFERENCES

1. D. J. Diner, R. A. Chipman, N. Beaudry, B. Cairns, L. D. Food, S. A. Macenka, T. J. Cunningham, S. Seshadri, and C. Keller, "An integrated multiangle, multispectral, and polarimetric imaging concept for aerosol remotesensing from space," *Proc. SPIE* **5659**, 88–96 (2005).
2. F. Snik, T. Karalidi, and C. U. Keller, "Spectral modulation for full linear polarimetry," *Appl. Opt.* **48**, 1337–1346 (2009).
3. W. Groner, J. W. Winkelman, A. G. Harris, C. Ince, G. J. Bouma, K. Messmer, and R. G. Nadeau, "Orthogonal polarization spectral imaging: a new method for study of the microcirculation," *Nat. Med.* **5**, 1209–1212 (1999).
4. T. G. Moran and J. M. Davila, "Three-dimensional polarimetric imaging of coronal mass ejections," *Science* **305**, 66–70 (2004).
5. R. S. Gurjar, V. Backman, L. T. Perelman, I. Georgakoudi, K. Badizadegan, I. Itzkan, R. R. Dasari, and M. S. Feld, "Imaging human epithelial properties with polarized light-scattering spectroscopy," *Nat. Med.* **7**, 1245–1248 (2001).
6. J. S. Tyo, D. L. Goldstein, D. B. Chenault, and J. A. Shaw, "Review of passive imaging polarimetry for remote sensing applications," *Appl. Opt.* **45**, 5453–5469 (2006).
7. K. Oka and T. Kato, "Spectroscopic polarimetry with a channeled spectrum," *Opt. Lett.* **24**, 1475–1477 (1999).
8. J. Li, J. P. Zhu, and H. Y. Wu, "Compact static Fourier transform imaging spectropolarimeter based on channeled polarimetry," *Opt. Lett.* **35**, 3784–3786 (2010).
9. J. S. Tyo and T. S. Turner, Jr., "Variable-retardance, Fourier-transform imaging spectropolarimeters for visible spectrum remote sensing," *Appl. Opt.* **40**, 1450–1458 (2001).
10. S. H. Jones, F. J. Iannarilli, and P. L. Kebabian, "Realization of quantitative-grade fieldable snapshot imaging spectropolarimeter," *Opt. Express* **12**, 6559–6573 (2004).
11. R. W. Aumiller, C. Vandervlugt, E. L. Dereniak, R. Sampson, and R. W. McMillan, "Snapshot imaging spectropolarimetry in the visible and infrared," *Proc. SPIE* **6972**, 697201 (2008).
12. J. C. Jones, M. W. Kudenov, M. G. Stapelbroek, and E. L. Dereniak, "Infrared hyperspectral imaging polarimeter using birefringent prisms," *Appl. Opt.* **50**, 1170–1185 (2011).
13. M. W. Kudenov, N. A. Hagen, E. L. Dereniak, and G. R. Gerhart, "Fourier transform channeled spectropolarimetry in the MWIR," *Opt. Express* **15**, 12792–12805 (2007).
14. J. Li, B. Gao, C. Qi, J. P. Zhu, and X. Hou, "Tests of a compact static Fourier-transform imaging spectropolarimeter," *Opt. Express* **22**, 13014–13021 (2014).
15. C. Zhang, Q. Li, T. Yan, T. Mu, and Y. Wei, "High throughput static channeled interference imaging spectropolarimeter based on a Savart polariscope," *Opt. Express* **24**, 23314–23332 (2016).
16. T. Mu, C. Zhang, C. Jia, and W. Ren, "Static hyperspectral imaging polarimeter for full linear Stokes parameters," *Opt. Express* **20**, 18194–18201 (2012).
17. C. Zhang, B. Xiangli, B. Zhao, and X. Yuan, "A static polarization imaging spectrometer based on a Savart polariscope," *Opt. Commun.* **203**, 21–26 (2002).
18. C. Zhang, B. Zhao, and B. Xiangli, "Wide-field-of-view polarization interference imaging spectrometer," *Appl. Opt.* **43**, 6090–6094 (2004).
19. K. Oka, "Stabilization of a channeled spectropolarimeter by self-calibration," *Opt. Lett.* **31**, 3279–3281 (2006).